Geophysical Journal International

Geophys. J. Int. (2013) doi: 10.1093/gji/ggs101

Geophysical Journal International Advance Access published January 10, 2013

Detection and modelling of the ionospheric perturbation caused by a Space Shuttle launch using a network of ground-based Global Positioning System stations

Timothy Bowling,[1] Eric Calais[2] and Jennifer S. Haase[3]

[1] *Department of Earth and Atmospheric Sciences, Purdue University, West Lafayette, IN, USA.*
[2] *Ecole Normale Supérieure, Laboratoire de Géologie, UMR8538, Paris, France.*
[3] *Institute of Geophysics and Planetary Physics, Scripps Institution of Oceanography, University of California, San Diego, La Jolla, CA, USA.*

Accepted 2012 December 4. Received 2012 November 30; in original form 2012 September 25

SUMMARY

The exhaust plume of the Space Shuttle during its ascent triggers acoustic waves which propagate through the atmosphere and induce electron density changes at ionospheric heights which changes can be measured using ground-based Global Positioning System (GPS) phase data. Here, we use a network of GPS stations to study the acoustic wave generated by the STS-125 Space Shuttle launch on May 11, 2009. We detect the resulting changes in ionospheric electron density, with characteristics that are typical of acoustic waves triggered by explosions at or near the Earth's surface or in the atmosphere. We successfully reproduce the amplitude and timing of the observed signal using a ray-tracing model with a moving source whose amplitude is directly scaled by a physical model of the shuttle exhaust energy, acoustic propagation in a dispersive atmosphere and a simplified two-fluid model of collisions between neutral gas and free electrons in the ionosphere. The close match between observed and model waveforms validates the modelling approach. This raises the possibility of using ground-based GPS networks to estimate the acoustic energy release of explosive sources near the Earth's surface or in atmosphere, and to constrain some atmospheric acoustic parameters.

Key words: Ionosphere/atmosphere interactions; Acoustic-gravity waves; Wave propagation.

1 INTRODUCTION

Sufficiently energetic atmospheric explosions are known to trigger infrasonic acoustic and gravity waves that can travel large distances (e.g. Yamamoto 1956; Widmer & Zürn 1992; Zürn & Widmer 1996). These waves can be directly observed with ground-based infrasound arrays (e.g. Brown *et al.* 2002), whose data can then be used to determine their source location and energy (e.g. Garces *et al.* 2004). As these perturbations propagate up to ionospheric heights, the neutral particle flow couples with the ionized plasma, inducing fluctuations of the ionospheric electron density. These perturbations can then be detected using a variety of ground- or space-based observation systems (Blanc 1985).

The Global Positioning System (GPS) provides a straightforward and relatively inexpensive way of measuring the ionospheric total electron content (TEC), as the inter-frequency delay of the signals transmitted from the satellite constellation to ground receivers is proportional to the integral of electron density along the line of sight path (Klobuchar 1985). Calais & Minster (1996) first showed the potential of this method to detect ionospheric perturbations caused by shallow earthquakes. Since then, powerful mine blasts (Calais *et al.* 1998), rocket ascents (Calais & Minster 1998; Afraimovich *et al.* 2002), volcanic explosions (Heki & Ping 2005; Dautermann *et al.* 2009a) and tsunamis (Artru *et al.* 2005; Occhipinti *et al.* 2006) have been detected using ground-based GPS measurements of the ionospheric TEC. The development of permanent networks of densely spaced and continuously recording GPS stations further allows for the investigation of such ionospheric perturbations at higher spatial and temporal resolution than currently possible with any other technique (Calais *et al.* 2003; Garrison *et al.* 2007).

The theories that link an explosive source to its associated atmospheric acoustic wave and the resulting ionospheric perturbation are relatively well known. Neutral flow can be simulated using ray tracing (e.g. Virieux 1996; Brokešová 2006) or normal mode summation (e.g. Lognonné *et al.* 1998; Kobayashi 2007; Dautermann *et al.* 2009b). Since viscous losses are near zero for acoustic waves with very low frequencies, their amplitude increases quasi-exponentially with decreasing atmospheric density so that energy is conserved. This amplification factor can reach 10^4 for near-surface sources. Therefore, atmospheric acoustic waves of relatively small amplitude at ground level can attain significant amplitude in the upper atmosphere. At ionospheric heights, the coupling between the neutral acoustic wave and free electrons can be calculated, assuming that charged particles follow the motion of neutral gas through collision

interactions (Davies & Archambeau 1998) using the Navier–Stokes equation of magneto-hydrodynamics (e.g. Boyd & Sanderson 2003; Kherani *et al.* 2008).

Dautermann *et al.* (2009a,b) applied these theories to model the ionospheric perturbation caused by the July 2003 Montserrat volcanic explosion and used GPS measurements of the associated TEC perturbation to estimate the explosion source energy. Here, we use a modified version of their approach to model the TEC perturbation caused by the May 11, 2009, STS-125 Atlantis space shuttle launch. The model is constrained by GPS data from a network of GPS stations in the Caribbean and along the eastern seaboard of the United States. We find that both the amplitude and timing of the observed signal are well reproduced using a moving point source, a dispersive atmosphere and a simplified two-fluid approach to electron excitation that only takes into account collisions between neutral gas and free electrons in the ionosphere.

2 THE STS-125 SPACE SHUTTLE LAUNCH

On May 11, 2009, the space shuttle Atlantis launched from Cape Canaveral, Florida, on mission STS-125. The shuttle lifted off at 18:01:55 UTC and initially followed a near-vertical trajectory until ejection of the solid rocket boosters (SRBs) at 18:04:00 (Fig. 1). It then continued to accelerate for about 5 min in near horizontal flight at an altitude between 90 and 120 km with a trajectory slightly north of east until main engine cutoff at 18:10:20 UTC (Fig. 2). At that point, the shuttle ejects its main fuel tank and translates its excess kinetic energy into altitude until reaching a final orbit at 559 km. During the acceleration phase, the expansion of super heated exhaust from the shuttle engine represents an energy source of about 2×10^{12} J. This triggers acoustic waves in the atmosphere, which eventually couple with free electrons and ions as they reach ionospheric height.

Perturbations of the ionospheric electron content caused by rocket launches have long been detected using ground-based measurements (e.g. Fehr 1968; Arendt 1971). Tolstoy *et al.* (1970) report a shock front propagating with a horizontal phase velocity of 700 to 800 m s^{-1} after an Apollo launch. More recently, Noble (1990) detected the ionospheric perturbation caused by the STS-4 space shuttle launch using incoherent scatter radar data from Arecibo. They found multiple arrivals of energy at different times, with dominant periods of 15 and 75 min, and determined that the most likely source region was coincident with the trajectory as it accelerates horizontally at about 110 km height. Jacobson & Carlos (1993) used ionospheric Doppler sounding data to study five space shuttle launches and report three successful detections of the associated ionospheric perturbation. They observed two arrivals separated by about 10 min, which they associated with the direct arrival of an acoustic wave and the reflected signal off the ground, respectively. Li *et al.* (1994) used very-long-baseline interferometry and the MARECS-B beacon satellite to observe Faraday rotation induced by space shuttle launches. They report ionospheric TEC perturbations up to 9.6×10^{23} electrons m^{-2} in amplitude, with dominant periods in the 50–150 s band.

Calais & Minster (1996) were the first to use GPS data to detect the ionospheric perturbation caused by a space shuttle launch. Their observation geometry had minimal spatial coverage, with one station and two detections. They report an acoustic perturbation with a dominant frequency of approximately 4 mHz and two arrivals separated by about 15 min. They speculated the second arrival to result from the ducting of the acoustic perturbation in a low-velocity waveguide between the mesopause and thermocline. A more recent study by Afraimovich *et al.* (2002), also using ground-based GPS data, showed similar results. These recent studies were, however, based on very few observations. In addition, they did not attempt to explain the observations through a physical model of the acoustic wave propagation and its coupling with the ionospheric plasma.

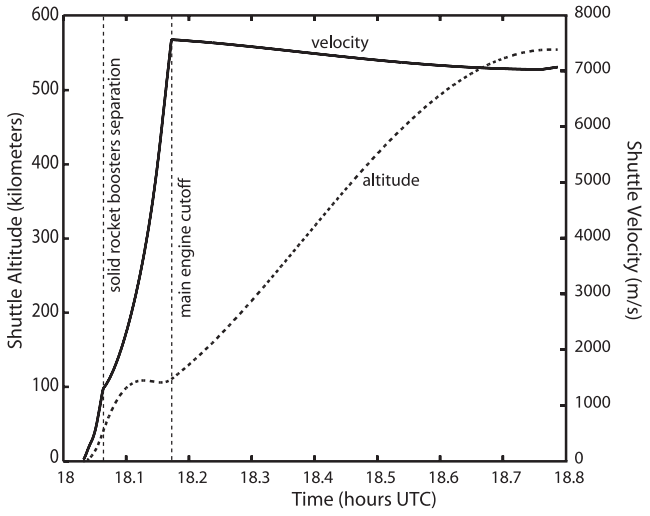

Figure 1. Profiles of the shuttle velocity (solid) and altitude (dashed) during ascent as a function of time. In order to maximize fuel efficiency, the shuttle ascends to approximately 100 km altitude, jettisons its SRBs and accelerates horizontally until main engine cut off. It then translates its excess kinetic energy into altitude until reaching its desired orbit. Most of the point source locations used in this work lie in the region of horizontal acceleration between 18:04:00 and 18:10:20 UTC.

3 DATA ANALYSIS

3.1 GPS trans-ionospheric sounding

The GPS constellation transmits on two frequencies in the L-band (f_1 = 1575.32 MHz and f_2 = 1227.60 MHz). As they propagate through the ionosphere, these signals experience a frequency-dependent phase advance that is proportional to the density of free electrons along the ray path (Klobuchar 1985). The path integral of electron density along the satellite–receiver line of sight, commonly referred to as TEC, can be directly computed from GPS phase observables Φ_1 and Φ_2 between satellite s and ground receiver r using

$$TEC_r^s = \left(\Phi_2 - \frac{f_1}{f_2}\Phi_1 + n + f_2(b_r + b^s)\right) \frac{f_1^2 f_2^2}{f_1^2 - f_2^2} \frac{c}{A}, \qquad (1)$$

where constant $A = 40.3$ m^3 s^{-2}, f_1 and f_2 are the carrier frequencies of the GPS signals and c is the speed of light (Calais & Minster 1996). Parameters n, b_r and b^s are phase ambiguities and hardware-specific code delays that can be estimated from the data (Mazzella *et al.* 2002; Ma & Maruyama 2003) for absolute TEC calculation. They are not considered in the present analysis because they are constant over a satellite arc and we are interested in relative variations of TEC rather than absolute TEC. All GPS stations used in this study were recording at a sampling interval of 30 s, which is therefore the sampling interval of the resulting TEC time series.

We isolate the acoustic perturbations of interest by filtering the raw TEC using a zero-phase fourth-order Butterworth filter with a passband between 2.1 mHz (the acoustic cutoff frequency calculated from the MSIS-E-90 atmosphere model; Hedin 1991) and 8 mHz

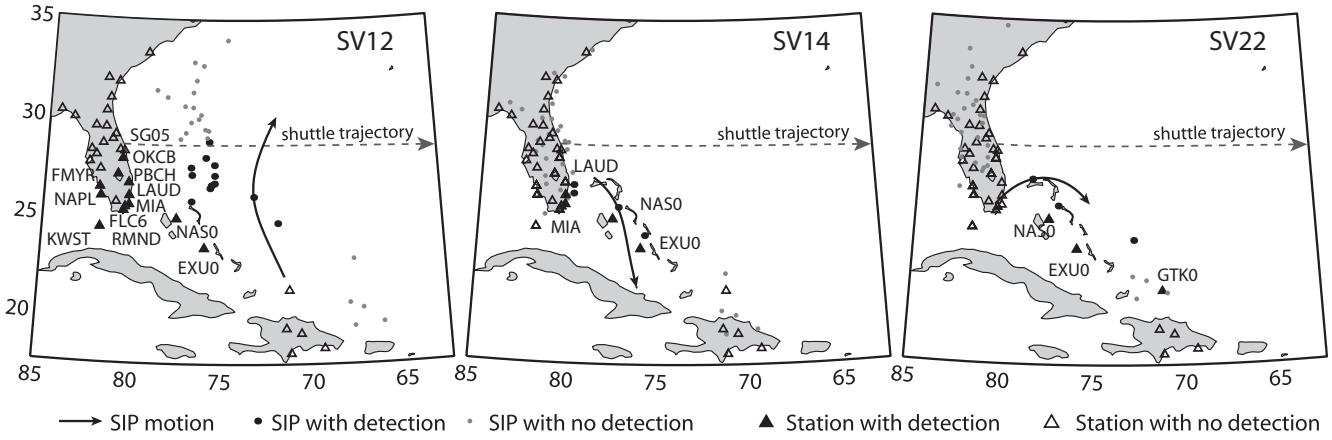

Figure 2. Map of the study area showing the observation geometry for satellites 12 (left), 14 (centre) and 22 (right). Unfilled triangles represent stations at which data were processed for all satellites and no detections found. Filled triangles represent stations exhibiting detections that are clearly above the background noise level. Black circles represent locations of the SIP (see Fig. 6) at time of first arrival. The grey circles represent the SIP locations at the expected time of arrival for stations with no detections. In order to give a sense of satellite motion, the solid black line shows the motion of the SIP for the NAS0-SV12 (left), 14 (centre) and 22 (right) receiver–satellite pairs. The dashed grey line shows the eastward shuttle trajectory.

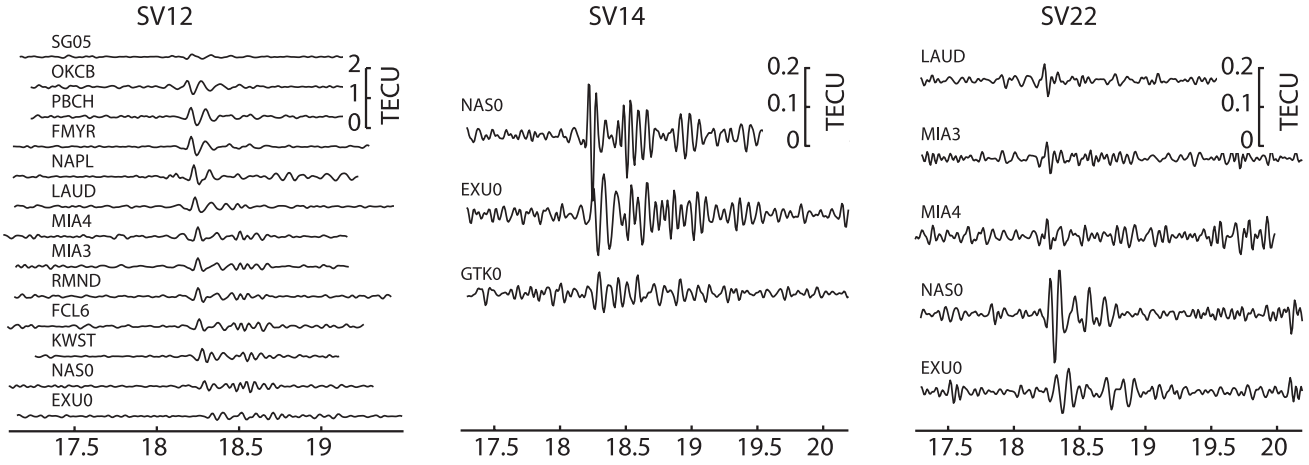

Figure 3. Strong detections for satellites 12 (left), 14 (centre) and 22 (right) and all stations, ordered from north (top) to south (bottom). The amplitude scale is given in the upper right corner of each panel (1 TECU = 10^{16} electrons m^{-2}). Note the amplitude scale difference between SV12 and SV14–SV22.

(the half Nyquist frequency for a GPS sampling rate of 30 s). We assign each TEC measurement to an ionospheric piercing point (IPP), defined as the intersection between the receiver–satellite line of sight and the altitude of greatest electron density (e_{max}). For this study, this altitude is 281 km, as determined from the International Reference Ionosphere at the time of the observations (Bilitza 2001). The projection of the IPP onto the Earth's surface is referred to as the sub-ionospheric point (SIP).

3.2 Observations

We use GPS data from 43 stations located along the eastern seaboard of the United States and in the northeastern Caribbean to calculate filtered TEC time series, as described above. This represents a total of 231 observations, given the GPS satellites available at the time of the STS-125 space shuttle launch. From this data set, we find clear detections of an ionospheric perturbation at the expected time for 14 GPS stations and three satellites (space vehicles (SV) 12, 14 and 22) (Fig. 2).

We extracted the shuttle position from the ascent/descent best estimate of trajectory (A/D BET) data product (Navigation & Flight Design Integration Group 2007). Position errors are fractions of a metre, much smaller than the relevant spatial scales of our work (sound speed $\times 30$ s).

The acoustic perturbations begin between 10 and 20 min after their corresponding point sources (Fig. 3), with a first arrival time that increases with distance from the source (point of closest approach between the shuttle track and the IPP, see below). Observations show an initial wave arrival characterized by oscillations periods around 180 s and amplitudes several times above the noise level. At some stations, a second arrival (second wave train) is detected about 15 min after the first one, with slightly lower periods. The spectrogram of the stacked signal at collocated stations MIA3 and MIA4 (Fig. 4) clearly shows these two distinct wave packets, separated by about 15 min. The first arrival has dominant frequencies between 2.5 and 5 mHz and most likely corresponds to the dominant acoustic modes of the atmosphere at 3.68 and 4.4 mHz (Watada 1995). The second wavetrain shows a slightly higher dominant frequency. Dautermann *et al.* (2009b) showed that this double wavetrain, reported after several atmospheric explosions, results from the beat of the dominant atmospheric modes and is not a source or reflection effect.

Plotted in the distance–time domain (Fig. 5), observations show a clear move out across the GPS array. Using a plane wave assumption,

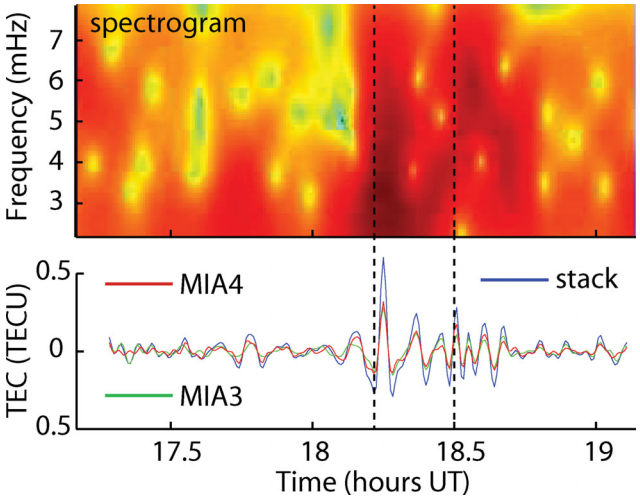

Figure 4. (Bottom) Filtered TEC time series for satellite 12 and colocated stations MIA3 (green) and MIA4 (red) and resulting stack (blue), which slightly increases the signal to noise ratio. (Top) Spectrogram of the stacked time series calculated using a Hamming window width of 30 min with a 29 min overlap. Two arrivals are clearly present in the detections with characteristic frequencies of ∼4 and ∼6 mHz, and are indicated by black dashed lines.

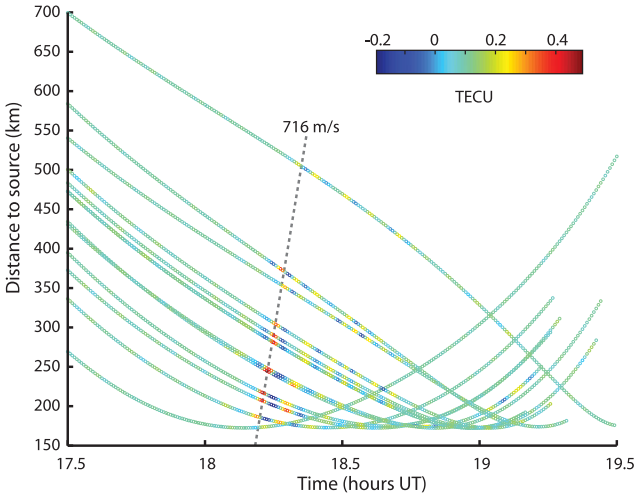

Figure 5. Detections for satellite 12 plotted in the distance–time domain. Each curve represents the distance of a given IPP from its corresponding point source. Colours represent the amplitude of filtered GPS-TEC signal. First arrivals cross the array with a clear move out velocity which can be fit as a plane wave with horizontal phase velocity of 716 m s^{-1}.

we find a best fit horizontal phase velocity for the first arrivals of 716 ± 73 m s^{-1} for satellite 12, 596 ± 123 m s^{-1} for satellite 14 and 632 ± 61 m s^{-1} for satellite 22. These phase velocities of ionospheric perturbations, similar to those found after other atmospheric explosions (Noble 1990; Li *et al.* 1994; Calais & Minster 1996; Afraimovich *et al.* 2002; Table 1), are consistent with sound speed in the upper atmosphere.

Peak-to-peak amplitudes range between 0.16 and 0.65 TECU (1 TECU = 10^{16} electrons m^{-2}), comparable to that obtained from previous studies of rocket launches (Table 1). Amplitudes do not show a simple relation with distance to the source because the efficiency of the coupling between the neutral wave and free electrons depends on the angle between the wave vector and the geomagnetic field vector. Electrons travel preferentially along magnetic field lines (Georges & Hooke 1970) so that the coupling can be described by cos(θ), where θ is the angle between the neutral wave vector and the magnetic field direction (Calais *et al.* 1998). Although many SIPs are located north of the shuttle track, these lie in an area where the wave vector is largely perpendicular to the magnetic field, hence where the coupling efficiency is low. This is evident in the low-amplitude TEC perturbation recorded for the SG05-SV12 receiver–satellite pair (Fig. 3), whose IPP is the closest to the shuttle track but also located north of it.

Overall, these observations are very similar to those reported by Calais & Minster after the STS-58 space shuttle launch, with much greater spatial resolution. Signals recorded on satellite 12, which show strong detections across 13 of the GPS stations, will serve as the basis for much of the modelling portion of this paper.

4 MODELLING

4.1 Theory

In order to simulate the ionospheric perturbations caused by the shuttle launch, we generalized the approach developed by Dautermann *et al.* (2009a) for a volcanic explosion point source to a moving point source. Indeed, because the speed of the shuttle is much greater than the speed of sound in the atmosphere, we can treat the wave to first order as quasi-cylindrically spreading with wave vectors perpendicular to the shuttle trajectory (Li *et al.* 1994). We can then approximate the source as the point of closest approach between the shuttle and the IPP (Calais *et al.* 1996).

We simulate the pressure wave by a set of 180 rays launched at takeoff angles from 0 to 90° (Fig. 6). The atmospheric refractive index, proportional to sound speed, is derived from the MSIS-E-90 atmospheric model (Hedin 1991). The ray tracing takes into account 2-D geometric spreading where, in an isotropic medium, acoustic intensity decreases as 1/R. This is accurate for a cylindrically spreading source, which the shuttle approximates due to its very high velocity.

We use an *N*-wave source function (first derivative of a Gaussian) following Afraimovich *et al.* (2002) and Dautermann *et al.* (2009a), described by

$$v(t) = (4\pi^{\frac{1}{2}}\sigma^3)^{-\frac{1}{2}} \frac{1}{2\sqrt{2}\sigma^2\pi^{\frac{1}{2}}}(t - t_o)e^{-\frac{(t-t_0)^2}{2\sigma^2}}, \quad (2)$$

Table 1. Comparison of different studies of acoustic waves produced by shuttle ascents.

Study	Amplitude [TECU]	Velocity [m s^{-1}]	Mission	Technique
Noble (1990)	N/A	628–735	STS-4	Incoherent Scatter Radar
Li *et al.* (1994)	0.0093–0.0703	600–700	STS-58, STS-60	VLBI
Calais and Minster. (1996)	0.039–0.25	862–894	STS-60	GPS
Afraimovich *et al.* (2002)	0.27–0.57	1529	STS-90, STS-95	GPS
This study	0.16–0.65	516–716	STS-125	GPS
Model	0.23–0.71	757	STS-125	GPS

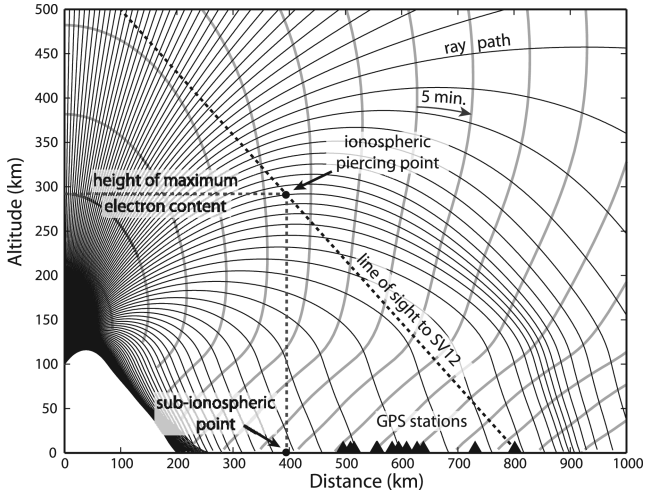

Figure 6. Ray tracing geometry for a single point source, in plane perpendicular to the shuttle trajectory. Black triangles show the projection of GPS stations onto this plane. The black dashed line shows the projection of the line of sight between a GPS station and satellite 12 onto this plane. The IPP and its projection onto the Earth's surface, or SIP, are indicated. Only the southern half of the modelled domain is shown. Solid black lines show rays produced by a source at 100 km altitude with takeoff angles above 31°. Rays with lower takeoff angles are trapped in the low-velocity channel between the mesopause and thermocline, or are reflected between the Earth's surface and the mesopause and are not shown here. Assuming a cylindrically spreading source, only ∼23 per cent of the source energy reaches the altitude of maximum electron content (281 km here). Grey lines locate the acoustic wavefront at 5 min intervals.

where v is the particle velocity of the neutral acoustic wave, t_o time of maximum displacement and σ the initial pulse width. We scale the input source amplitude by

$$C = \int_{-\infty}^{+\infty} v^2(t)\,\mathrm{d}t, \tag{3}$$

where C is a constant. We calculate C using a physical model of the acoustic waves produced by a shuttle ascent. Li *et al.* (1994) show that the acoustic pressure overburden for a cylinder of hot expanding gas (shuttle exhaust) is given by

$$p_{\mathrm{acoustic}} = 2.75 p_o \frac{V_o}{V_{\mathrm{shuttle}}}, \tag{4}$$

where V_{shuttle} is the speed of the space shuttle, V_o the shuttle exhaust speed (≈3.2 km s^{-1}; Li *et al.* 1994) and p_o the ambient pressure. Acoustic pressure p and particle velocity are related via the specific acoustic impedance Z of the material (Ford 1970) following

$$Z = \frac{p}{v} = \rho c, \tag{5}$$

where ρ is the air density at the altitude considered. We can relate the maximum particle velocity of the N wave to the maximum pressure p_o (or pressure overburden) using

$$v_{\max} = \frac{2.75 p_o}{\rho c} \frac{V_o}{V_{\mathrm{shuttle}}}. \tag{6}$$

Parameters ρ, c and p_o are obtained or derived for a given altitude from spatially and temporally specific atmospheric reference models. Once scaled, we can numerically integrate eq. (3) to obtain a value for C.

Dauterman *et al.* (2009a) showed that the propagation of the neutral wave requires accounting for atmospheric dispersion, with the time evolution of the pulse width that can be approximated as $\sigma(t) = \sqrt{a + bt}$. Parameter a describes the initial width of the pulse, while b describes the broadening of the pulse as the acoustic wave propagates. Following Dautermann *et al.* (2009a), we set the initial pulse width at $a = 1$ s, scale the source function as described above for each individual satellite–receiver pair based on the shuttle velocity and the altitude at the point source, and allow b to vary in order to best fit the observations. This leads to the shape and amplitude of the synthetic waveform, which we calculate at the intersection between rays and satellite–receiver lines-of-sight.

We then calculate the electron density perturbation caused by the neutral pressure wave using a simplified two fluid version of the Navier–Stokes magneto-hydrodynamic equation (Boyd & Sanderson 2003):

$$\rho_{\mathrm{e}} \frac{\mathrm{d}\vec{v}_{\mathrm{e}}}{\mathrm{d}t} = -\nabla p + \rho_{\mathrm{e}}\vec{g} + Ne(\vec{v}_{\mathrm{e}} \times \vec{B}) - \rho_{\mathrm{e}} \nu_{\mathrm{en}}(\vec{v}_{\mathrm{e}} - \vec{u}), \tag{7}$$

which relates the electron particle velocity $\vec{v}_{\mathrm{e}}$ to the neutral particle velocity $\vec{u}$ via electron mass density ρ_{e}, pressure p, gravity $\vec{g}$, electron density N, electron charge e and electron-neutral collision frequency ν_{en}. ν_{en} is calculated as a function of electron temperature and neutral gas density (Dautermann *et al.* 2009a). We use an electron density profile from the International Reference Ionosphere (Bilitza 2001) to calculate N and the International Geomagnetic Reference Field (Maus & Macmillan 2005) to obtain $\vec{B}$. We finally integrate the electron density perturbations computed at every intersection between acoustic rays and satellite–receiver lines-of-sight to obtain the synthetic signal that we compare to the observed, GPS-derived, TEC perturbation.

4.2 Results

We applied the aforementioned model to the calculated point source for each receiver with strong detections by satellite 12. The sound velocity, electron density and geomagnetic field are derived from reference climatological models and are specific to the latitude, longitude, date and time of the observations.

The ray tracing shows that only a portion of source energy propagates to the altitude of $e_{\max}$ (about 281 km), typical of the ray pattern produced in a medium where sound speed increases with height (Ford 1970). Waves with takeoff angles between 43° and 90° reach or exceed $e_{\max}$, gradually turning towards the horizontal and bending back towards the Earth. Waves with takeoff angles between 31° and 43° propagate upward but are bent back towards Earth before reaching $e_{\max}$. Below 31°, rays are either ducted in the low-velocity channel between the mesopause and thermocline, or are reflected between the Earth's surface and the mesopause. Because a significant portion of the initial source energy does not propagate to detectable altitudes, models that fail to take into account a realistic sound speed profile for the atmosphere are likely to underestimate the initial source amplitude by several orders of magnitude.

As mentioned above, we varied parameter b so as to best match the synthetic waveforms to the observed ones. The fit between observed and modelled TEC time series is quantified using the following chi-squared function:

$$\chi^2 = \sum_{i=1}^{M} \left(\frac{y_i - y(b)}{\sigma_i}\right)^2, \tag{8}$$

where M is the total number of samples, y_i is the envelope of the observed signal, $y(b)$ the envelope of the modelled signal and σ_i the measurement uncertainty. We assumed a constant measurement

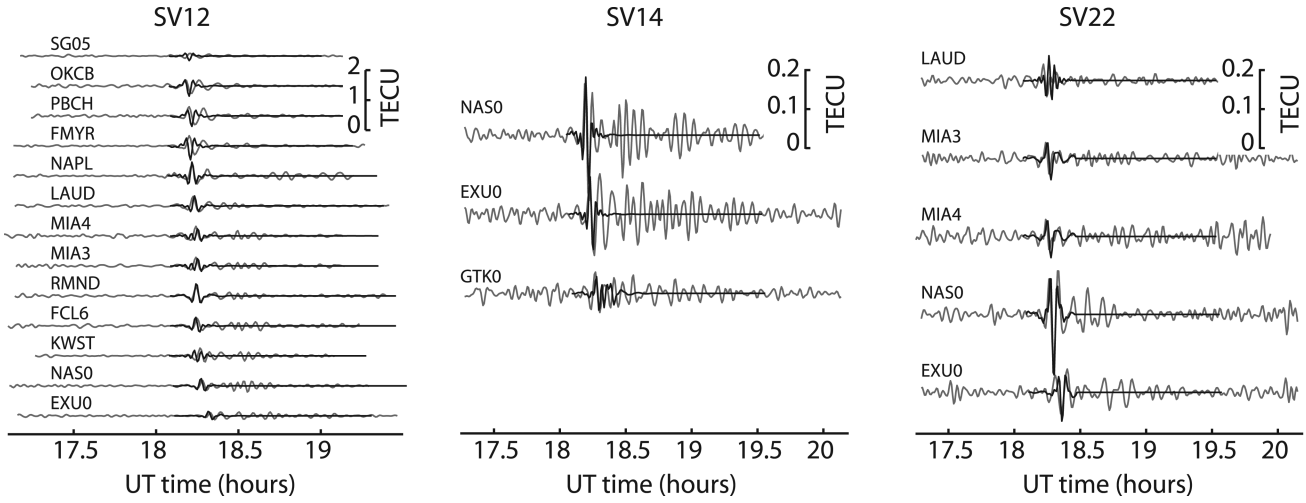

Figure 7. Calculated (black) and observed (grey) waveforms for satellites 12 (left), 14 (centre) and 22 (right). The amplitude scale is given in the upper right corner of each panel (1 TECU = 10^{16} electrons m^{-2}). Note the amplitude scale difference between SV12 and SV14–SV22.

error $\sigma_i = 0.0249$ TECU, derived from the variance of the observed TEC signal in the 2.2–8 mHz frequency range in the absence of the acoustic perturbation.

The best fit (Fig. 7) is obtained for $b = 0.131$, close to the value found by Dautermann *et al.* (2009a) for a volcanic explosion ($b = 0.128$). The resulting model waveforms match the observed ones well. Since we are using a point source model to synthesize the acoustic wave produced by a moving source, we are, however, limited to reproducing the initial part of the waveform. Its later evolution is likely to reflect processes unaccounted for in the model, such as a source more complex than the simple *N* wave used here, waves arriving from different locations along the shuttle track, waves ducted through low-velocity zones of the atmosphere, unmodelled lateral variations in the sound speed profile, or excitations of lower velocity modes of the atmosphere.

The peak-to-peak amplitudes of modelled detections range from 0.23 to 0.71 TECU, with a mean difference of 0.067 TECU from observed values. The calculated amplitude evolution across the array matches well that of the observations. The timing of first arrivals closely fits observations as well, with a maximum difference of 120 s and a mean of 27 s. The simulated wave moves across the GPS array with a horizontal phase velocity of 757 ± 92 m s^{-1}, close to the observed move-out velocity (Fig. 8). We applied the same model parameters for satellite 12 (including parameter *b* defined above) to detections on satellites 14 and 22 and found a similar agreement between simulated and observed waveforms (Fig. 7).

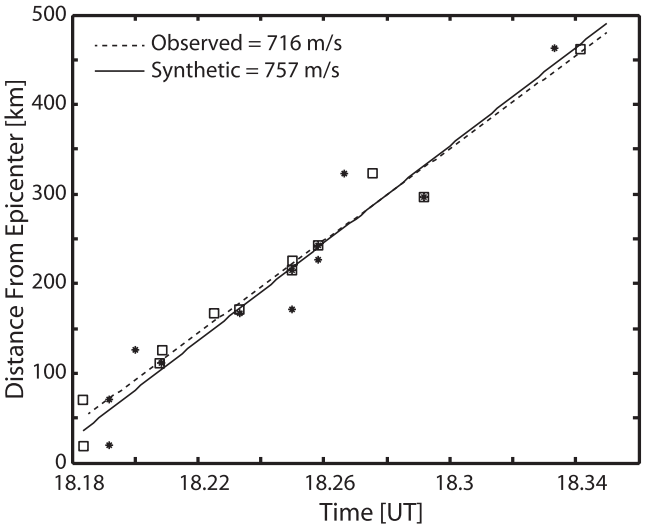

Figure 8. Distance from the source at the time of first arrival (stars = model, squares = observed) and best fit move-out velocities using a plane wave assumption plotted for the calculated (solid line) and observed (dashed line) waves. The model fit has a slightly later origin time than the observations, but a faster wave speed, resulting in a very small difference at most sites.

5 DISCUSSION

5.1 Model uncertainties

Modelling results in this work are sensitive to several input parameters. The electron density as a function of altitude ($e(z)$) determines the height of the IPP, hence the location of point source, which, in turn, maps into the source function amplitude. Inaccuracies in $e(z)$ therefore affect both the arrival time and amplitude of the model results. To first order, a change Δz in the altitude of e_{max} corresponds to horizontal change of IPP location of $\Delta x = \Delta z / \tan\theta_e$ where θ_e is the satellite–receiver elevation angle. For example, for satellite 12, a change of ±10 per cent in the altitude of e_{max} (28.1 km) modifies the horizontal location of the IPPs by about 50 km, the arrival time by about 70 s and the signal amplitude by ±3 per cent.

Our modelling procedure uses a 1-D atmosphere with sound speed derived from temperature assuming hydrostatic equilibrium (Beer 1974). It does not account for lateral heterogeneities, or wind (which can reach up to 100 m s^{-1} in the upper atmosphere), which would both affect the ray tracing. Using the HWM-93 empirical wind model (Hedin *et al.* 1996), we, however, find that horizontal wind speed at the altitude of e_{max} is only 8.3 per cent of the sound speed. We ran our model with a sound speed profile altered by ±8.3 per cent and found, for satellite 12, arrival times that varied at most by ±56 s, depending on the distance from source to detection. Therefore, uncertainties in the MSIS-E-90 sound speed and International Reference Ionosphere models used here do not significantly affect our results.

The model also neglects the contribution of shock waves produced by the supersonic motion of the shuttle, whose amplitude depend on the shape, mass and velocity of the vehicle. In an ideal gas, the dynamic pressure of a supersonic shockwave varies as $p_o M^2$ where p_o is the ambient pressure and *M* is the Mach number

(Clancy 1975). Because pressure increases as the square of velocity, it is probable at high speeds that the dynamic pressure due to the supersonic shock would be greater than the pressure overburden due to the expansion of shuttle exhaust. However, non-linear shock waves decay rapidly with distance (Clancy 1975) and do not provide an accurate estimate of what the initial amplitude of the acoustic wave that propagates to far field should be. Additionally, it is likely, although not explicitly stated, that the Li *et al.*'s (1994) source model used here is calibrated to match the total acoustic energy release of the shuttle during ascent (including both exhaust and shock components).

Finally, our model only takes into account electron-neutral particle interactions, neglecting ion-electron and neutral-ion interactions which may play an important role in inducing free electron oscillations in the ionosphere (Kherani *et al.* 2008). This can occur in two ways: neutral-ion collisions followed by ion-electron collisions; and neutral-ion collisions inducing localized currents which, in turn, result in free electron flows. The former may be negligible because the rate of neutral-ion collisions in the ionosphere is two orders of magnitude lower than the rate of neutral-electron or electron–ion collisions. The effects of induced currents in relation to this study are currently unquantified, but we speculate that the results would be (1) a delay introduced in the synthetic TEC signal relative to current arrival times, which likely would not be significant for the 30 s sampling interval used here, and (2) an increase in amplitude of the observed oscillations. Nonetheless, the close match in amplitude (greater than 90 per cent) and timing of observations implies that a simplified two-fluid approach neglecting the electric field is suitable to simulate GPS-TEC signals caused by explosions in the experimental geometry used here.

5.2 Model verification

Dautermann *et al.* (2009a) developed the ray-tracing modelling approach on which we based our work in order to estimate the energy released by a volcanic explosion. However, they had no independent way of verifying the accuracy of their result. Here, we know the source energy *a priori* from a physical model of the excitation of acoustic waves by a rocket exhaust plume, with maximum pressures determined by the vehicle velocity, altitude and exhaust exit velocity. The very good fit in the arrival time and amplitude between the simulated and observed signals described above validates the method developed by Dautermann (2009a), in spite of its simplifications. This also implies that the method can be used to accurately estimate the acoustic energy release of explosive sources via GPS observations of the ionosphere. Consequently, this method could be used to determine the optimal location of GPS receivers for the purpose of detecting and characterizing explosive sources (for example, around suspected nuclear test sites), or to estimate the minimum energy release detectable in given atmospheric conditions, for a given observation network geometry.

The best fit value for the atmospheric dispersion parameter b found in this work (0.131) is close to that found by Dautermann *et al.* (2009) (0.128). This suggests that these values represent an intrinsic physical property of atmospheric dispersion. The dispersion of atmospheric acoustic waves depends on molecular relaxation absorption, viscous losses and thermal conduction (Bass *et al.* 2009). Relaxation absorption dominates in regimes where the acoustic wavelength is greater than the molecular mean free path (as is the case in this study). This effect is dependent on the ratio of molecular species, temperature and ambient pressure (Sutherland & Bass 2004). This opens the possibility that GPS detection of acoustic waves of known origin, timing and amplitude could be used to constrain atmospheric dispersion characteristics, providing an empirical basis with which to study the upper atmosphere. Further studies are required to validate this approach and possibly derive a physical basis for model parameter b. This would strengthen the ability of ground-based GPS observations to characterize energetic acoustic events at or near the Earth's surface.

6 CONCLUSIONS

We have used a network of ground-GPS stations to detect the acoustic perturbation caused by the STS-125 Space Shuttle ascent via its effect on the ionospheric electron content. The data set used here is superior to that used in all previous studies of rocket or shuttle launches because it allowed us to observe and quantify the signal move out across the array and the variations of its amplitude as a function of both distance to the source and observation geometry in relation to the geomagnetic field.

We have successfully reproduced the amplitude and timing of the observed signal using a ray-tracing model derived from Dautermann *et al.* (2009), with a moving source whose amplitude is directly scaled by a physical model of shuttle exhaust energy, a dispersive atmosphere and a simplified two-fluid approach that only takes into account collisions between neutral gas and free electrons in the ionosphere. The close match between observed and model waveforms indicates that the modelling assumptions, although fairly simple, are consistent with the data. This raises the possibility of using ground-based GPS networks to estimate the acoustic energy release of explosive sources near the Earth's surface or in atmosphere, and to constrain some atmospheric acoustic parameters.

Because rocket launches are constrained to periods of atmospheric quiescence, the effects of atmospheric wind and temporal variations in atmospheric parameters are minimized. In addition, parameters such as rocket track and launch time are well documented. Finally, networks of continuously operating GPS stations are rapidly expanding in North America and the Caribbean (e.g. http://coconet.unavco.org). Space Shuttle or other rocket launches therefore provide a unique experimental setting in which to test and refine the technique of GPS-TEC detection and modelling of atmospheric acoustic waves. Despite the recent conclusion of the shuttle program, there are a wealth of well documented and unanalysed shuttle launches that will hopefully provide future use to the aeronomy community.

ACKNOWLEDGMENTS

We thank Thomas Dautermann for his help implementing the ray-tracing method to the case of a moving source. We are grateful to William Haase at the Kennedy Space Center for providing us the shuttle flight information and to two anonymous reviewers for their constructive comments.

REFERENCES

Afraimovich, E.L., Kosogorov, E.A. & Plotnikov, A.V., 2002. Shock-acoustic waves generated during rocket launches and earthquakes. *Cosmic Res.,* **40,** 241–254.

Arendt, P.R., 1971. Ionospheric undulations following Apollo 14 launching, *Nature,* **231,** 438–439.

Artru, J., Ducic, V., Kanamori, H., Lognonné, P. & Murakami, M., 2005. Ionospheric detection of gravity waves induced by tsunamis, *J. geophys. Int.,* **160,** 840–848.

Bass, H.E., Hetzer, C.H. & Raspet., R., 2009. On the speed of sound in the atmosphere as a function of altitude and frequency, *J. geophys. Res.,* **114**(D15110), doi:10.1029/2006JD007806.

Beer, T., 1974. *Atmospheric Waves,* Wiley, New York.

Bilitza, D., 2001. International Reference Ionosphere 2000, *Radio Sci.,* **36,** 261–276.

Blanc, E., 1985. Observations in the upper atmosphere of infrasonic waves from natural or artificial sources: a summary, *Ann. Geophys.,* **3**(6), 673–688.

Boyd, T.J.M. & Sanderson, J.J., 2003. *The Physics of Plasmas,* Cambridge Univ. Press, Cambridge, United Kingdom.

Brokešová, J., 2006. *Asymptotic Ray Method in Seismology: A Tutorial,* Matfyzpress, Prague, Czech Republic.

Brown, D.J., Katz, C.N., Le Bras, R., Flanagan, M.P., Wang, J. & Gault, A.K., 2002. infrasonic signal detection and source location at the prototype International Data Centre, *Pure appl. Geophys.,* **159,** 1081–1125.

Calais, E. & Minster, J.B., 1996. GPS detection of ionospheric perturbations following a Space Shuttle ascent, *Geophys. Res. Lett.,* **23,** 1897–1900.

Calais, E. & Minster, J.B., 1998. GPS, earthquakes, the ionosphere, and the Space Shuttle, *Phys. Earth planet. Inter.,* **105,** 167–181.

Calais, E., Haase, J.S. & Minster, J.B., 2003. Detection of ionospheric perturbations using a dense GPS array in Southern California, *Geophys. Res. Lett.,* **30**(12), doi:10.1029/2003GL017708.

Calais, E., Minster, J.B., Hofton, M.A. & Hedlin, M.A.H., 1998. Ionospheric signature of surface mine blasts from Global Positioning System measurements, *J. geophys. Int.,* **132,** 191–202.

Clancy, L.J., 1975. *Aerodynamics*. Wiley, New York.

Dautermann, T., Calais, E. & Mattioli, G., 2009a. Global Positioning System detection and energy estimation of the ionospheric wave caused by the 13 July 2003 explosion of the Soufriere Hills Volcano, Montserrat, *J. geophys. Res.,* **114**(B02202), doi:10.1029/2008JB005722.

Dautermann, T., Calais, E., Lognonné, P. & Mattioli, G., 2009b. Lithosphere-atmosphere-ionosphere coupling after the 2003 explosive eruption of the Soufriere Hills Volcano, Montserrat, *J. geophys. Int.,* **176,** 1–13.

Fehr, U., 1968. Propagating energy into the upper atmosphere including lower ionosphere generated by artificial sources, in *Acoustic-Gravity Waves in the Atmosphere: Symposium Proceedings,* ed. Georges, T.M., U.S. Government Printing Office, Washington, D.C.

Ford, R.D., 1970. *Introduction to Acoustics,* Elsevier, Amsterdam and New York.

Garces, M. *et al.*, 2004. Forensic studies of infrasound from massive hypersonic sources, *EOS, Trans. Am. geophys. Un.,* **85,** 433, doi:10.1029/2004EO430002.

Garcia, R., Crespon, F., Ducic, V. & Lognonné, P., 2005. Three-dimensional ionospheric tomography of post-seismic perturbations produced by the Denali earthquake from GPS data, *J. geophys. Int.,* **163,** 1049–1064.

Garrison, J.L., Lee, S.C.G., Haase, J.S. & Calais, E., 2007. A method for detecting ionospheric disturbances and estimating their propagation speed and direction using a large GPS network, *Radio Sci.,* **42**(RS6011), doi:10.1029/2007RS003657.

Georges, T. & Hooke, W., 1970. Wave-induced fluctuations in ionospheric electron content: a model indicating some obervational biases, *J. geophys. Res.,* **75,** 6295–6308.

Hedin, A.E., 1991. Extension of the MSIS thermosphere model into the middle and lower atmosphere, *J. geophys. Res.,* **96,** 1159–1172.

Hedin, A.E. *et al.*, 1996. Empirical wind model for the upper, middle and lower atmosphere, *J. Atmos. Terr. Phys.,* **58,** 1421–1447.

Heki, K. & Ping, J., 2005. Directivity and apparent velocity of the coseismic ionospheric disturbances observed with a dense GPS array, *Earth planet. Sci. Lett.,* **236,** 845–855.

Jacobson, A.R. & Carlos, R.C., 1993. Observations of acoustic-gravity waves in the thermosphere following Space Shuttle ascents, *J. Atmos. Terr. Phys.,* **56,** 525–528.

Kherani, E.A., Lognonné, P., Kamath, N., Crespon, F. & Garcia, R., 2008. Response of the ionosphere to seismic trigerred acoustic waves: electron density and electromagnetic fluctuations, *J. geophys. Int.,* **176,** 1–13.

Klobuchar, J.A., 1985. *Handbook of Geophysics and the Space Environment,* Chapter 10.8, pp. 1084–1088, ed. Jursa, A.S., U.S. Air Forces, Washington, D.C.

Kobayashi, N., 2007. A new method to calculate normal modes, *Geophys. J. Int.,* **168,** 315–331.

Li, Y.Q., Jacobson, A.R., Carlos, R.C., Massey, R.S., Taranenko, Y.N. & Wu, G., 1994. The blast wave of the Shuttle plume at ionospheric heights, *Geophys. Res. Lett.,* **21,** 2737–2740.

Lognonné, P., Clévédé, E. & Kanamori, H., 1998. Computation of seismograms and atmospheric oscillations by normal-mode summation for a spherical earth model with realistic atmosphere, *J. geophys. Int.,* **135,** 388–406.

Ma, G. & Maruyama, T., 2003. Derivation of TEC and estimation of instrumental biases from GEONET in Japan, *Ann. Geophys.,* **21**(10), 2083–2093.

Maus, S. & Macmillan, S., 2005. International geomagnetic reference field - the tenth generation, *Earth Planets Space,* **57,** 1135–1140.

Mazzella, A.J., Holland, E.A., Andreasen, A.M., Rao, G.S. & Bishop, G.J., 2002. Autonomous estimation of plasmasphere content using GPS measurements, *Radio Sci.,* **37,** doi:10.1029/2001RS002520.

Navigation & Flight Design Integration Group. (2007). Internal interface control document: ascent/descent BET product, Report #ICD-I-TOP-003 Rev. D.

Noble, S.T., 1990. A large-amplitude traveling ionospheric disturbance excited by the Space Shuttle during launch, *J. geophys. Res.,* **95**(A11), 19 037–19 044.

Occhipinti, G., Lognonné, P., Kherani, E.A. & Hébert, H., 2006. Three-dimensional waveform modeling of ionospheric signature induced by the 2004 Sumatra tsunami, *Geophys. Res. Lett.,* **33,** L20104, doi:10.1029/2006GL026865.

Sutherland, L.C. & Bass, H.E., 2004. Atmospheric absorption in the atmosphere up to 160 km, *J. acoust. Soc. Am.,* **115,** 3, doi:10.1121/1.1631937.

Tolstoy, I., Montes, H., Rao, G. & Willis, E., 1970. Long-period sound waves in the thermosphere from Apollo launches, *J. geophys. Res.,* **75,** 5621–5625.

Virieux, J., 1996. Seismic ray tracing, in *Seismic Modelling of Earth Structure,* pp. 223-303, eds Boschi, E., Ekström, G. & Morelli, A., Inst. Naz. Geofis., Rome, Italy.

Watada, S., 1995. Part 1: near source acoustic coupling between the atmosphere and the solid earth during volcanic erruptions, *PhD thesis,* California Institute of Technology.

Widmer, R. & Zürn, W., 1992. Bichromatic excitation of long-period Rayleigh and air waves by the Mount Pinatubo and El Chicón volcanic eruptions, *Geophys. Res. Lett.,* **19,** 765–768.

Yamamoto, R., 1956. The microbarographic oscillations produced by the explosion of hydrogen bombs in the Marshall islands, *Bull. Am. Met. Soc.,* **37,** 406–409.

Zürn, W. & Widmer, R., 1996. Worldwide observation of Bichromatic long-Period Rayleigh waves excited during the June 15th, 1991 eruption of Mount Pinatubo, in *Fire and Mud: Eruptions and Lahars of Mount Pinatubo, Philippines,* pp. 615–624, ed. Punongbayan, R.S. & Newhall, C.G., Univ. of Washington Press, Seattle.